Active Site Reactant Center Geometry in the Co^{II}−Product Radical Pair State of Coenzyme B_{12}-Dependent Ethanolamine Deaminase Determined by Using Orientation-Selection Electron Spin−Echo Envelope Modulation Spectroscopy

Jeffrey M. Canfield and Kurt Warncke*

Department of Physics, Emory University, Atlanta, Georgia 30322

Received: August 24, 2004; In Final Form: November 10, 2004

The distances and orientations among reactant centers in the active site of coenzyme B_{12}-dependent ethanolamine deaminase from *Salmonella typhimurium* have been characterized in the Co^{II}−product radical pair state by using X-band electron paramagnetic resonance (EPR) and two-pulse electron spin−echo envelope modulation (ESEEM) spectroscopies in the disordered solid state. The unpaired electron spin in the product radical is localized on C2. Our approach is based on the orientation−selection created in the EPR spectrum of the biradical by the axial electron−electron dipolar interaction. Simulation of the EPR line shape yielded a best-fit Co^{II}−C2 distance of 9.3 Å. ESEEM spectroscopy performed at four magnetic field values addressed the hyperfine coupling of the unpaired electron spin on C2 with ^2H in the C5′ methyl group of 5′-deoxyadenosine and in the β-^2H position at C1 of the radical. Global ESEEM simulations (over the four magnetic fields) were weighted by the orientation dependence of the EPR line shape. A Nelder−Mead direct search fitting algorithm was used to optimize the simulations. The results lead to a partial model of the active site, in which C5′ is located a perpendicular distance of 1.6 Å from the Co^{II}−C2 axis, at distances of 6.3 and 3.5 Å from Co^{II} and C2, respectively. The van der Waals contact of the C5′-methyl group and C2 indicates that C5′ remains close to the radical species during the rearrangement step. The C2−H_s−C5′ angle including the strongly coupled hydrogen, H_s, and the C5′−H_s orientation relative to the C1−C2 axis are consistent with a linear hydrogen atom transfer coordinate and an in-line acceptor p-orbital orientation. The trigonal plane of the C2 atom defines sub-spaces within the active site for C5′ radical migration and hydrogen atom transfers (side of the plane facing Co^{II}) and amine migration (side of the plane facing away from Co^{II}).

Introduction

Ethanolamine deaminase is a bacterial coenzyme B_{12} (adenosylcobalamin, Figure 1) dependent enzyme[1] (also known as ethanolamine−ammonia lyase) that catalyzes the elimination of ammonia from aminoethanol **1** to produce acetaldehyde **4**.[2] The key steps in the reaction are mediated by radical species. As depicted in Figure 2, homolytic cleavage of the cobalt−carbon bond of coenzyme B_{12} produces low-spin ($S = {}^1/_2$) Co^{II} in cobalamin, and a C5′-centered 5′-deoxyadenosyl radical species that is proposed to initiate catalysis in all coenzyme B_{12}-dependent enzymes.[3−5] Hydrogen atom abstraction from the carbinol carbon (C1) of the bound substrate by the C5′ radical generates the C1-centered substrate radical **2**,[6,7] and the C5′-methyl group in 5′-deoxyadenosine. The substrate radical then rearranges to a product radical, with the unpaired electron spin density localized on C2.[8] Subsequent hydrogen atom transfer from the C5′ methyl group to C2 of the product radical yields a diamagnetic product species and re-forms the 5′-deoxyadenosyl radical. The 5′-deoxyadenosyl radical and Co^{II} may then recombine.[9] The structures of five coenzyme B_{12}-dependent enzymes, including free and substrate-, inhibitor-, or product-bound states, have been determined by X-ray crystallography.[10−19] These states may contain Co^{II},[20] but apparently not organic radical species. Structural information about the reactant centers in the unstable Co^{II}−radical pair intermediate states has been revealed by high-resolution techniques of electron paramagnetic resonance (EPR) spectroscopy, applied to disordered samples of cryotrapped Co^{II}−radical pair intermediates.[21−23] Here, we apply the combined experimental and simulation approach of orientation-selection electron spin−echo envelope modulation (ESEEM)[23] spectroscopy to determine the three-dimensional geometry of Co^{II}, the C5′-methyl group and the C1−C2 product radical frame in the Co^{II}−product radical pair intermediate in ethanolamine deaminase from *Salmonella typhimurium*.[24,25]

The product radical accumulates during steady-state turnover on the native substrate, aminoethanol, and is stabilized for low-temperature spectroscopy by cryotrapping.[8] EPR simulation analysis of the product radical line shape showed that the Co^{II}−C2 distance in the Co^{II}−product radical pair is 9.7 Å,[26] which is comparable to the best-fit value of 9.3 Å (range 8.5−10.5 Å) that we report here. The Co^{II}−C2 distance is slightly shorter than the Co^{II}−C1 distances of 10−12 Å,[27] 11 Å,[7] and 11.1 Å (range 10.9−11.5 Å)[23] reported by different groups for the Co^{II}−substrate radical pair state. A carbinolamine (1-aminoethan-1-ol-2-yl) structure **3** for the product radical was determined from differences in the EPR line shape of the product radical generated from ^{14}N- or ^{15}N-labeled aminoethanol.[28] The radical rearrangement step therefore proceeds by the amine migration pathway, in which the amine nitrogen migrates from C2 to C1 to form **3**.[28] Multifrequency three-pulse powder ESEEM of the hyperfine interactions between the product radical and the ^2H-labeled C5′-methyl group showed coupling with the C5′−^2H at effective separations of 2.3 Å (one ^2H) and 4.2 Å (two ^2H).[29]

* Corresponding author. Tel: 404-727-2975. Fax: 404-727-0873. E-mail: kwarncke@physics.emory.edu.

10.1021/jp046167m CCC: $30.25
Published on Web 01/25/2005

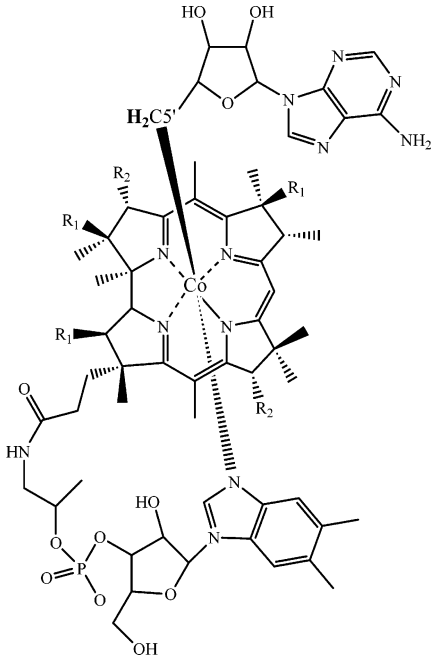

Figure 1. Depiction of the structure of vitamin B_{12} coenzyme [adenosylcob(III)alamin or adenosylcobalamin]. The X-ray crystallographic structures of cobalamins have been reviewed.[66,67] The β-axial ligand is the 5′-deoxyadenosyl group (above page plane) and the α-axial ligand is 5,6-dimethylbenzimidazole (below page plane). The coenzyme retains dimethylbenzimidazole as an α-axial ligand when bound in ethanolamine deaminase.[68,69] R_1 and R_2 refer to acetamide and propionamide side chains. The C5′ carbon of 5′-deoxyadenosyl is labeled, and the two exchangeable hydrogen atoms on the coenzyme are shown in bold.

CHART 1

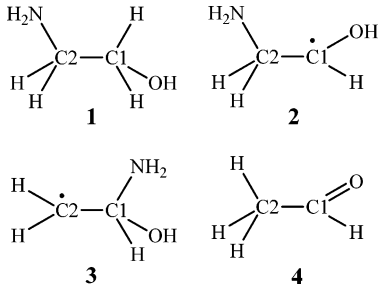

These results led to a model in which the C2−C5′ distance was 3.3 ± 0.1 Å.[29] Hyperfine interactions of the C2 unpaired electron spin with the β-^{2}H at C1 revealed two types of β-^{2}H coupling, which led to the proposal of two different C1−C2 rotamer states for the product radical.[28,29] The powder three-pulse ESEEM did not, however, report on the three-dimensional orientation among Co^{II}, C2, C1, and the C5′ methyl group, which remains to be elucidated.

We have introduced and described the approach of orientation-selection spectroscopy for the case of radical pair systems,[23] in which the orientation-selection in the EPR line shape arises from the electron−electron dipolar interaction. Different magnetic field values across the line shape correspond to subpopulations of orientations of the electron−electron vector (**R**) relative to the external magnetic field vector ($\mathbf{B}_0$). The orientations contributing to the spectrum at any magnetic field value can be calculated from simulations of the EPR spectrum. ESEEM collected at a particular magnetic field is representative of the corresponding subpopulation of orientations. The electron−nuclear interactions that give rise to the ESEEM include an anisotropic contribution from the dipolar interaction that is

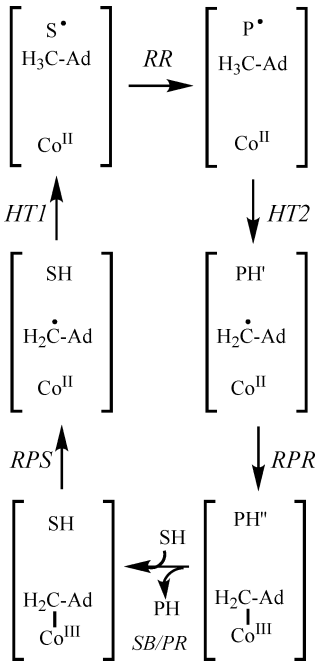

Figure 2. Minimal mechanism for catalysis in vitamin B_{12} coenzyme-dependent enzymes.[5] The forward direction of reaction is indicated by the arrows. In ethanolamine deaminase, the detectable reversibility of individual steps varies among different substrates.[70] The brackets represent the active site region in the protein interior. Substrate-derived species are designated S−H (substrate), S• (substrate radical), P• (product radical), PH′, PH″ (bound product species), and PH (free products). The 5′-deoxyadenosyl β-axial ligand is represented as Ad−CH_2− in the intact coenzyme, and as Ad−CH_2• (5′-deoxyadenosyl radical) or Ad−CH_3 (5′-deoxyadenosine) following cobalt−carbon bond cleavage. The cobalt ion and its formal oxidation states are depicted, but the corrin ring and α-axial ligand of the coenzyme are not shown for clarity. Steps of the cycle are denoted RPS (radical pair separation), HT1 (first hydrogen atom transfer), RR (radical rearrangement), HT2 (second hydrogen atom transfer), RPR (radical pair recombination), and SB/PR (substrate binding/product release).

sensitive to the orientation of the electron−nuclear vector relative to the external magnetic field. Therefore, the orientation of the electron−electron and electron−nuclear vectors can be determined by using the EPR simulations to weight the contribution of different orientations to the ESEEM. Global simulation of the ESEEM collected at different magnetic field values then reveals the orientations of the nuclei relative to the electron−electron axis. We have implemented a Nelder-Mead Simplex direct search optimization algorithm[30,31] to automate fitting. The experimental and theoretical approaches are related to the orientation-selection ENDOR[32−35] and ESEEM[36] spectroscopies in transition metal systems, where the orientation selection is created primarily by anisotropy in the *g*-tensor.

For the present studies, the product radical was cryotrapped during steady-state turnover on aminoethanol-1,1,2,2-$^2H_4$ ($^2H_4$-aminoethanol) or natural abundance ($^1H_4$-)aminoethanol. The multiple turnovers of the enzyme prior to sample cryotrapping result in the rapid and complete exchange of ^{2}H into all three sites of the C5′ methyl group of 5′-deoxyadenosine.[37] In addition, the nonsolvent-exchangeable hydrogen atoms on the product radical (1,1,2,2-positions) are ^{2}H labeled. The hyperfine coupling parameters for the three C5′-^{2}H and the β-^{2}H have been previously determined in the powder three-pulse ESEEM study.[29] The strong coupling of the two equivalent α-deuterons[38] places it outside of the microwave pulse bandwidth detection limit of the ESEEM technique.[39−41] In addition, the three-pulse study established that the stronger of the two β-^{2}H hyperfine

couplings is detected at a microwave frequency/magnetic field value of 10.89 GHz/388.0 mT but is not detected above the noise level at the lower X-band frequency/field of 8.86 GHz/313.0 mT.[29] In concurrence with this result, the stronger β-^{2}H coupling (denoted $H_{\beta 2}$) was not observed in the two-pulse ESEEM studies performed at 8.77 GHz that are reported here, whereas features from the weaker β-^{2}H coupling (denoted $H_{\beta 1}$) are prominent.

The magnetic interactions of the unpaired electron at C2 with ^{2}H nuclei were measured at four magnetic field values by using the two-pulse ESEEM technique.[39−41] Global simulation analysis of the ^{2}H-ESEEM reveals the orientation of the three C5′ methyl hydrogen and β-hydrogen positions relative to the Co^{II}−C2 axis. A model for the three-dimensional geometry of the ^{2}H nuclei, C2, C1, C5′, and Co^{II} is presented. The model provides insights into the mechanism of radical-mediated catalysis in ethanolamine deaminase.

Experimental Procedures

Enzyme Preparation. Enzyme was purified from the *Escherichia coli* overexpression strain incorporating the cloned *S. typhimurium* ethanolamine deaminase coding sequences[24] essentially as described,[24] with the exception that the enzyme was dialyzed against buffer containing 100 mM HEPES (pH 7.45), 10 mM KCl, 5 mM dithiothreitol, 10 mM urea, and 10% glycerol.[42] Enzyme activity was determined as described[43] by using the coupled assay with alcohol dehydrogenase/NADH. The specific activity of the purified enzyme with aminoethanol as substrate was 25−35 μmol/min/mg.

Sample Preparation. Adenosylcobalamin (Sigma Chemical Co.), aminoethanol-1,1,2,2-$^2H_4$ ($^2H_4$-aminoethanol; Cambridge Isotope Laboratories, Inc.) and natural abundance aminoethanol (Aldrich Chemical Co.) were purchased from commercial sources. The reactions were performed in air-saturated buffer containing 100 mM HEPES (pH 7.5), 10 mM KCl, and 5 mM dithiothreitol. Identical results were obtained with air-saturated and anaerobic samples. All manipulations were carried out on ice under red safe-lighting. The product radical was generated by using a procedure for fast cryotrapping of steady-state intermediate states in ethanolamine deaminase.[8] The final concentration of enzyme was 10−15 mg/mL, which is equivalent to 20−30 μM for a holoenzyme molecular mass of 500 000 g/mol.[25] Adenosylcobalamin was added to 120−180 μM, which is stoichiometric with active sites. The active site/holoenzyme stoichiometry of 6 is based on adenosylcobalamin titrations of substrate radical formation (K. Warncke, unpublished) and is in agreement with the value obtained by two separate methods.[44,45] The procedure for specific incorporation of ^{2}H into the hydrogen positions of the C5′ carbon in enzyme-bound adenosylcobalamin has been described in detail.[22] Turnover of the enzyme on $^2H_4$-aminoethanol leads to exchange of ^{2}H into the C5′ hydrogen positions of the coenzyme.[22] Following mixing of the enzyme−substrate solution with adenosylcobalamin, the sample was loaded into a 4 mm o.d. EPR tube, and the tube was plunged into liquid nitrogen-chilled isopentane ($T \approx 130$ K) to trap the Co^{II}−product radical pair state. The total elapsed time from mixing to isopentane immersion was approximately 15 s.

Continuous-Wave EPR Spectroscopy. EPR spectra were obtained by using a Bruker ER200D EPR spectrometer equipped with a Bruker 4102ST TE102 cavity, HP 4256L frequency counter, Varian V3603 electromagnet, and Fieldial Mark I regulator/power supply, and Air Products cryostat and temperature controller modified for nitrogen gas flow sample cooling.

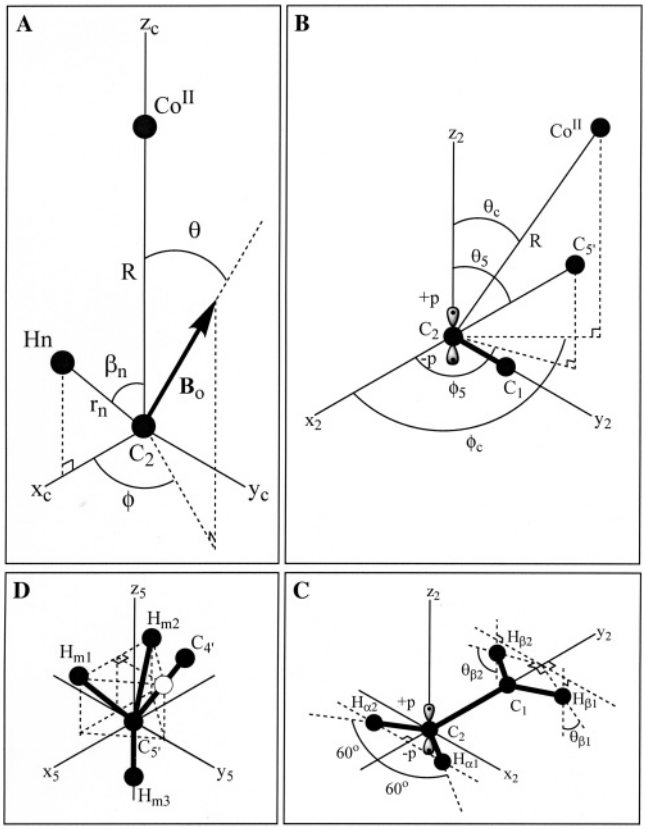

Figure 3. Coordinate systems used to define the relative positions of Co^{II}, C2, C1, C5′, and the C5′ methyl hydrogen atoms, and the α- and β-hydrogen atoms of the product radical in the active site of ethanolamine deaminase. (A) The $x_cy_cz_c$ coordinate system used to define the orientation of the magnetic field vector (B_0) with polar and azimuthal angles, θ and ϕ, relative to the active site in EPR and ESEEM simulations. Hydrogen site, H*n*, lies a distance, r_n, from the unpaired electron spin on C2, and β_n is the angle between the C2−H*n* bond axis and the C2−Co^{II} axis. (B) The $x_2y_2z_2$ coordinate system, which positions the C2−C1 bond axis and the C2 p-orbital relative to C5′ and Co^{II}. (C) Detail of the $x_2y_2z_2$ coordinate system, showing the positions of the α- and β-hydrogens on the product radical. (D) The $x_5y_5z_5$ coordinate system, which positions the C5′-methyl hydrogen sites relative to the C5′ center. The open circle shows the position of a fourth hydrogen position in an open tetrahedron, which is occupied by the ribose C4′ atom in the 5′-deoxyadenosyl group.

ESEEM Data Acquisition and Processing. ESEEM was collected by using the two-pulse microwave pulse sequence.[39−41] Envelope modulation was dead time-reconstructed[46] and cosine Fourier transformed to generate ESEEM frequency spectra. All data processing was done using locally written Matlab code (Matlab v. 6.5 and Matlab Compiler v. 3.0) on Windows PC's.

Theory

Coordinate Systems. Figure 3 shows the coordinate systems that were used to specify the orientations and separation distances among the atom centers. The $x_cy_cz_c$ coordinate system used for EPR and ESEEM simulations is shown in Figure 3A. The polar (θ) and azimuthal (ϕ) angles describe the orientation of the magnetic field vector $\mathbf{B}_0$ in spherical coordinates. The coupled hydrogen sites (either ^{2}H or ^{1}H) are denoted as H*n* in the calculations, where $n = 1-7$. The three C5′ methyl hydrogen sites correspond to $n = 1-3$ and are denoted in Figure 3 as H_{m1}, H_{m2}, and H_{m3}. The two α-H bonded to C2 are denoted as $H_{\alpha 1}$ and $H_{\alpha 2}$, and the two types of β-H bonded to C1 are denoted as $H_{\beta 1}$ and $H_{\beta 2}$. Each H*n* is treated as if it lies in the x_cz_c plane a distance r_n from C2, because the EPR spin Hamiltonian (eq

10) is axial about z_c and all orientations θ, ϕ of $\mathbf{B}_0$ are sampled in the powder average. The H*n*−C2−Co^{II} angle for each hydrogen is denoted β_n. The C2−Co^{II} vector can be reversed without altering the simulated ESEEM, so that β_n and 180° − β_n give the same ESEEM waveform. Therefore, only β_n values from 0 to 90° are considered.

To obtain the β_n and r_n values for ESEEM calculations, the atom positions are calculated and the following expressions are used:

$$r_n = |\overrightarrow{\mathrm{C2-H}n}| \tag{1}$$

$$-\cos(\beta_n) = \frac{\overrightarrow{\mathrm{Co^{II}-C2}}\cdot\overrightarrow{\mathrm{C2-H}_n}}{|\overrightarrow{\mathrm{Co^{II}-C2}}||\overrightarrow{\mathrm{C2-H}_n}|} = \frac{\overrightarrow{\mathrm{Co^{II}-C2}}\cdot\overrightarrow{\mathrm{C2-H}_n}}{R\cdot r_n} \tag{2}$$

Additional coordinate systems are used to position the different H*n* sites on the product radical and C5′ methyl group. Figure 3B shows the $x_2y_2z_2$ coordinate system, which positions C5′, Co^{II}, C1, C2 and the lobes (denoted "+p" and "−p") of the p-orbital on C2. Figure 3C presents another view of the $x_2y_2z_2$ coordinate system, which highlights the positions of the product radical atoms relative to C2. The two α-hydrogens ($H_{\alpha1}$ and $H_{\alpha2}$) on C2 are placed in the x_2y_2 plane and oriented symmetrically about the y_2z_2 plane. Two different β-hydrogen sites[28] are defined, as follows: $H_{\beta1}$, with $x_2 \geq 0$ and $H_{\beta2}$, with $x_2 \leq 0$, both with $z_2 \leq 0$ and $y_2 \geq 1.44$ Å. This constrains C2−$H_{\beta n}$ to a range of 1.81−2.54 Å, because standard bond lengths are used for C1−C2 (1.44 Å) and C−H (1.1 Å) in the product radical. The positions of the $H_{\beta n}$ in the $x_2y_2z_2$ coordinate system were determined from the $H_{\beta n}$ isotropic hyperfine coupling. This determination, and the origin of the two β-hydrogen sites, is described under ESEEM simulations, below. Figure 3D shows the orientation of the C5′ methyl group H atoms within the $x_5y_5z_5$ coordinate system. The C5′−H_{mn} distances and inter-hydrogen bond angles are fixed at 1.1 Å and 109.5°, respectively, corresponding to sp^3-hybridization at C5′. In Figure 3D, the fourth C5′ bonding position is shown to be occupied by the C4′ carbon of the ribose moiety.

Powder Averaging and Angle Selection. Powder averaging was used in simulations of the EPR and ESEEM spectra from the frozen solutions used in this study. If $f(\theta,\phi)$ is the EPR spectrum that a single crystal would give for $\mathbf{B}_0$ oriented in the θ, ϕ direction with respect to the crystal's $x_cy_cz_c$ axes, then the powder average is given by

$$\langle f(\theta,\phi)\rangle = \frac{\int_0^{\pi}\sin(\theta)\,\mathrm{d}\theta\int_0^{2\pi}\mathrm{d}\phi\, f(\theta,\phi)}{\int_0^{\pi}\sin(\theta)\,\mathrm{d}\theta\int_0^{2\pi}\mathrm{d}\phi} \tag{3}$$

Similarly, if $F(\theta,\phi)$ is the ESEEM waveform that a single crystal would give, the powder-averaged ESEEM waveform is given by an expression comparable to eq 3, as follows:

$$\langle F(\theta,\phi)\rangle = \frac{\int_0^{\pi}\sin(\theta)\,\mathrm{d}\theta\int_0^{2\pi}\mathrm{d}\phi\, F(\theta,\phi)}{\int_0^{\pi}\sin(\theta)\,\mathrm{d}\theta\int_0^{2\pi}\mathrm{d}\phi} \tag{4}$$

To account for the orientation selection of the ESEEM, the factor, $P(\theta,\phi)$, which reflects the relative population or relative EPR absorption transition intensity, at each orientation, θ, ϕ, enters eq 4 as follows:

$$\langle F(\theta,\phi)\rangle = \frac{\int_0^{\pi}\sin(\theta)\,\mathrm{d}\theta\int_0^{2\pi}\mathrm{d}\phi\, F(\theta,\phi)\,P(\theta,\phi)}{\int_0^{\pi}\sin(\theta)\,\mathrm{d}\theta\int_0^{2\pi}\mathrm{d}\phi\, P(\theta,\phi)} \tag{5}$$

In practice, the orientation averaging is approximated numerically by summing over a finite set of orientations θ_j, ϕ_j.[23]

Fitting Procedures. The experimental EPR and ESEEM spectra were fitted by using the Nelder−Mead simplex direct search method[30,31] as implemented in Matlab's "fminsearch" algorithm. This algorithm minimizes a fitting function, σ, that reflects the goodness-of-fit between an experimental curve (the data points Y_j) and a calculated curve (the points x_j). The calculated curve is given by the following general expression

$$y_j = Ax_j + B \tag{6}$$

In eq 6, the coefficient A scales the range of x_j whereas B accounts for a constant "baseline" contribution. The fitting function, σ, is given by the squared deviation of Y_j and y_j, as follows:

$$\sigma = \sum_j (Y_j - y_j)^2 = \sum_j [Y_j - (Ax_j + B)]^2 \tag{7}$$

The following first derivative expressions for $\mathrm{d}\sigma/\mathrm{d}A$ and $\mathrm{d}\sigma/\mathrm{d}B$ were solved to find the set of A, B values that gave the smallest σ value for a particular set of experimental Y_j and calculated x_j.

$$\frac{\mathrm{d}\sigma}{\mathrm{d}A} = \sum_j (2Ax_j^2 - 2x_jY_j + 2Bx_j) = 0 \qquad \text{where}$$

$$\frac{\mathrm{d}^2\sigma}{\mathrm{d}A^2} = \sum_j (2x_j^2) \geq 0 \tag{8A}$$

$$\frac{\mathrm{d}\sigma}{\mathrm{d}B} = \sum_j (2B - 2Y_j + 2Ax_j) = 0 \qquad \text{where}$$

$$\frac{\mathrm{d}^2\sigma}{\mathrm{d}B^2} = \sum_j (2) \geq 0 \tag{8B}$$

Details of the fitting procedure have been presented previously.[23]

To fit the experimental $^2H/^1H$ quotient ESEEM waveforms, a modification of eqs 6−8 was used. The calculated curve, $z_j(\tau_j)$, where τ_j is the dephasing time in the two-pulsed ESE sequence, was multiplied by $e^{k\tau_j}$ to obtain

$$x_j = z_j(\tau_j)e^{k\tau_j} \tag{9}$$

The factor $e^{k\tau_j}$ corrects for any differences between the individual ^2H and ^1H echo envelopes caused by irreversible loss of spin coherence. In the individual envelopes, the envelope decay is quasi-exponential and governed by the phase memory time, T_M. Thus, for a $^2H/^1H$ quotient ESEEM waveform, $k = (1/T_{M,1H}) - (1/T_{M,2H})$.

EPR Simulations. The program MENO[47] was used to simulate the EPR spectra. The program treats spin Hamiltonians, such as those previously reported for radical pairs in different coenzyme B_{12}-dependent enzymes,[27] that contain axial dipolar interaction terms, isotropic exchange terms (J), an axial $\mathbf{g}$ tensor, and axial hyperfine tensors ($\mathbf{A}$). The Hamiltonian in the $x_cy_cz_c$ coordinate system is written as follows,

$$H = h[-J\vec{S}_1\cdot\vec{S}_2 + A_\perp(S_{1x}I_{1x} + S_{1y}I_{1y}) + A_{||}S_{1z}I_{1z}] + (\vec{\mu}_1 + \vec{\mu}_2)\cdot\vec{B}_0 + \frac{\mu_0}{4\pi}\left[\frac{\vec{\mu}_1\cdot\vec{\mu}_2}{R^3} - \frac{3(\vec{\mu}_1\cdot\vec{R})(\vec{\mu}_2\cdot\vec{R})}{R^5}\right] \quad (10)$$

where

$$\vec{\mu}_j = \beta_e(g_{jx}S_{jx}\hat{x} + g_{jy}S_{jy}\hat{y} + g_{jz}S_{jz}\hat{z}) \quad (11)$$

The subscripts "1" and "2" correspond to Co^{II} and the radical, respectively.

In the simulations, $\boldsymbol{R}$ is along z_c, $g_{1x} = g_{1y} = g_\perp = 2.26$ and $g_{1z} = g_{||} = 2.01$, $g_{2xyz} = 2$,[27,45] $S_1 = S_2 = 1/2$, and $I_1 = 7/2$. The cobalt hyperfine parameters are $A_\perp = 30$ MHz (10×10^{-4} cm^{-1}) and $A_{||} = 309$ MHz (103×10^{-4} cm^{-1}).[27] The sign convention for J in MENO is that $J < 0$ indicates antiferromagnetic coupling and thus corresponds to a lower energy for the singlet relative to the triplet state.[47] Different isotropic Gaussian line widths were used for the Co^{II} and radical contributions to the spectrum to account for the different relaxation behavior and unresolved hyperfine couplings for each electron.[6] To optimize the fit, J, R, and the line widths were varied from a variety of initial parameter sets to minimize σ as specified in eq 7, with Y_j from the experimental spectra and x_j from the direct output from MENO. Although both J and R contribute to the magnitude of the doublet splitting in the radical line shape, R also determines the anisotropic part of the dipolar interaction, and thus influences the line width of each radical doublet feature. Agreement between simulations performed with MENO, and simulations performed with the frequency-based, direct-diagonalization method of the program, DSNANI,[48] shows that the perturbation series used to derive MENO holds well for the radical pair Hamiltonian used here and in previous studies.[23]

A series of EPR absorption spectra were calculated for each θ value, and cross-sections of the EPR transition intensity versus orientation at the particular values of 306.5, 310.5, 313.3, and 319.0 mT were taken. The corresponding spectra and cross-sections are shown in Figures 5 and 6, respectively. The cross section at each field was rescaled to have a maximum of 1, and each resulting cross section (as shown in Figure 6) was denoted as $P(\theta,\phi)$. Because the area under an EPR absorption spectrum can be used to measure the spin population,[38] the resultant $P(\theta,\phi)$ curves were then used to weight the powder average, as given in eq 5, when calculating the ESEEM spectra. In the absence of orientation selection, $P(\theta,\phi) = 1$ would hold, and a normal powder average, as given by eq 4, would result.

ESEEM Simulations. *Individual Electron−Nuclear Couplings*. The ESEEM simulation approach was based on Mims' formalism.[49,50] The implementation of this approach has been described.[22,51] The simulations focused on the coupling of the unpaired electron spin on C2 with hydrogen sites on the C5′ methyl group and on the product radical. Each hydrogen site, Hn, was parametrized by r_n and β_n, as defined in Figure 3A, and $A_{iso,n}$, the isotropic hyperfine coupling. The ESEEM from hydrogen site Hn was calculated by using the spin Hamiltonian

$$H = \beta_e g_e \vec{B}_0\cdot\vec{S}_2 - \beta_N g_N \vec{B}_0\cdot\vec{I}_2 + h\vec{S}_2\cdot\vec{\vec{A}}_2\cdot\vec{I}_2 \quad (12)$$

where $g_e = 2$, $S_2 = 1/2$, $g_N = 5.5857$ for ^{1}H and 0.8574 for ^{2}H, $I_2 = 1/2$ for ^{1}H and 1 for ^{2}H, and $\vec{\vec{A}}_2$ is the complete hyperfine tensor. The nuclear quadrupole interaction terms for the $I_2 = 1$ ^{2}H nucleus were neglected because they are generally small compared to the hyperfine couplings and had little influence on simulations in preliminary work.

TABLE 1: Best-Fit EPR Simulation Parameters and Fit Numbers

input parameters	best-fit values[a]	best-fit range[b]	
$J/10^{-4}$ cm^{-1}	−67.2	−70.8	−63.7
J/MHz	−202	−212	−191
R/Å	9.26	8.49	10.50
radical line width/mT	5.16	4.79	5.67
Co^{II} line width/mT	6.08	4.53	8.03
g(radical)	2.000	1.998	2.001
$g_\perp(Co^{II})$	2.260	2.249	2.265
$g_{||}(Co^{II})$	2.010	1.987	2.032
$A_\perp/10^{-4}$ cm^{-1} (Co^{II})	10	4.78	14.77
$A_{||}/10^{-4}$ cm^{-1} (Co^{II})	103	88.95	105.72
fitting parameters	**best-fit values**	**best-fit range**	
$\sigma_{EPR}/10^{29}$	1.19	1.19	2.00

[a] The best-fit values were obtained by optimizing J, R, and the line widths, with g value and hyperfine parameters held fixed at literature values. [b] The minimum and maximum values for each parameter represent the range obtained when the indicated parameter was varied with all of the other parameters held fixed at their best-fit values. These extreme values reflect the parameter range in which σ_{EPR} remained $\leq 2.00 \times 10^{29}$.

The model of Gordy[52] for the interaction between an unpaired electron spin in a p-orbital and a nuclear spin was adapted for the treatment of the hyperfine interactions, with the exception of the α-H. In the Gordy model, the electron spin density is concentrated equally at effective centers of the p-orbital lobes, 0.72 Å above and below the nodal plane, and the dipole interactions between Hn and each lobe are summed. The complete (including both isotropic and dipolar contributions) rhombic tensor for the α-hydrogen hyperfine couplings was given explicitly ($A_{2xyz} = [-58, -91, -29]$ MHz for ^{1}H coupling and $A_{2xyz} = (g_D/g_H)[-58, -91, -29]$ MHz for ^{2}H coupling, where $g_D = 0.8574$ and $g_H = 5.5857$.[38] The $A_{iso,\beta 2}$ and $r_{\beta 2}$ parameters were also given explicitly by the values determined by multifrequency three-pulse ESEEM (see Table 2).[28,29] The $H_{\beta 2}$ parameters were not adjustable, because the ESEEM from the $H_{\beta 2}$ coupling is not detectable above the noise level at the microwave frequency/magnetic field values used in the present study.[29] The ESEEM from the $H_{\beta 1}$ coupling was observed, as expected,[29] and therefore, the $A_{iso,\beta 1}$ and $r_{\beta 1}$ parameters were adjustable. For each site $H_{\beta n}$, the dihedral angle between the p-orbital axis and the C1−$H_{\beta n}$ bond, $\theta_{\beta n}$, was calculated from the fitted value of the isotropic hyperfine coupling by using the Heller−McConnell relation:[53] $A_{iso,\beta n} = \rho B_2 \cos^2\theta_{\beta n}$, where $\rho = 1$ is the unpaired electron spin density at C2,[8] and $B_2 = 24.9$ MHz for ^{2}H.[54]

The hyperfine tensor for each Hn site, $\vec{\vec{A}}_2$, was rotated into the $x_c y_c z_c$ coordinate system, and the ESEEM from each orientation was weighted as in eq 5 by using $P(\theta)$, the θ-dependence obtained from the EPR simulation. This allowed the treatment of effects on the ESEEM caused by J and R without explicitly including these terms in the spin Hamiltonian of eq 12.

The powder average for each of the seven individual coupled hydrogen sites, Hn (in both the ^{2}H and ^{1}H occupied states), was calculated independently, as in eq 5.[39,41,55] Owing to the large number of powder average orientations to sample for each Hn site and multiple parameters to vary during optimization, Mims' expressions[49] for the envelope modulation from a single site at a single orientation were rearranged into the following form:

$$E(\tau) = \sum_q A_q e^{i\omega_q\tau} \quad (13)$$

where A_q includes τ-independent amplitude terms and $e^{i\omega_q\tau}$ is

TABLE 2: Best-Fit ESEEM Simulation Parameters and Ranges Obtained from Global Fitting of the ESEEM Collected at Four Different Magnetic Field Values[a]

variable	best-fit value	best-fit range	
R/Å	9.26	fixed	
r(C2−C5′)/Å	3.48	3.05	3.55
r(Co^{II}−C5′)/Å[e]	6.34	5.88	6.82
	12.47	12.18	12.67
C5′−H_a−C2/deg	161	143	180
$A_{iso,a}$/MHz	−0.75	−0.79	−0.66
$A_{iso,\beta1}$/MHz	4.57	4.48	4.66
$A_{iso,\beta2}$/MHz	7.8	fixed	
r_a/Å[b]	2.42	2.09	2.46
r_b/Å[b]	4.07	3.67	4.11
r_c/Å[b]	4.09	3.72	4.21
$r_{\beta1}$/Å[c]	2.44	2.37	2.52
$r_{\beta2}$/Å[d]	2.37	fixed	
β_a/deg[b]	20.8	2.51	29.5
β_b/deg[b]	21.6	0.103	42.8
β_c/deg[b]	26.1	0.199	39.7
$\beta_{\beta1}$/deg[c]	56.2	44.4	83.3
$\beta_{\beta2}$/deg[d]	62.3	38.6	89.9
global fit number	**best-fit value**	**best-fit range**	
$(\Sigma\sigma_t)(\Pi\sigma_f)/10^{14}$	1.86	1.86	2.17

[a] The best-fit range column lists ranges from more than 70 000 separate fitting attempts (simulation runs). From the best-fit global fit number corresponding to the results in Figures 7 and 8, a best fit range (listed at the bottom of the Best Fit Range column) was selected. Simulation runs with global fit numbers within this range were used to determine the ranges for each parameter. Thus, if r(C2−C5′) is in the range listed, a global fit with a fit number within the best-fit range can be achieved by using a combination of all of the other fitting parameters from within their respective ranges. Plots of the fit values versus the range for different parameters are shown in Figure S1. [b] The r_a, r_b, r_c and β_a, β_b, β_c parameters are related to the r_{m1}, r_{m2}, r_{m3} and β_{m1}, β_{m2}, β_{m3} parameters but sorted so that $r_a \le r_b \le r_c$ holds. Thus, H_a is the strongly coupled hydrogen, H_s, and H_b and H_c are the weakly coupled hydrogens, H_w. [c] The $A_{iso,\beta1}$, $r_{\beta1}$, and $\beta_{\beta1}$ parameters refer to the observed β-^{2}H coupling with $H_{\beta1}$, with $p_{\beta1} = p_{\beta2} = 0.5$, as given in eqs 14−16. [d] The $A_{iso,\beta2}$, $r_{\beta2}$, and $\beta_{\beta2}$ parameters refer to the population of β-^{2}H coupling with $H_{\beta2}$, which is not observed under the experimental conditions used here. The $r_{\beta2}$ parameter is fixed by the value reported in ref 29, and $p_{\beta1} = p_{\beta2} = 0.5$, as given in eqs 14−16. [e] Inversion symmetry of the model leads to two possible values for each of the Co^{II}−C5′ and Co^{II}−C1 distances.

the τ-dependent propagator.[39,41,56] In this form, the exponential terms are evaluated as infrequently as possible over the range of τ values. The Matlab Compiler (v. 3.0) was also used to speed this portion of the code, which was the main bottleneck for the calculations.

Combination of Electron−Nuclear Couplings. The total two-pulse ESEEM for a group of nuclei interacting with the same electron is given by the product of the ESEEM obtained separately from each nucleus.[49,57] Thus, the simulated total ESEEM waveform was obtained by powder-averaging the ESEEM (eq 5) from each nucleus separately, followed by multiplication of the individual powder-averaged ESEEM waveforms.[58,59] The total ESEEM waveform from the ^{2}H-labeled sample is given as follows:

$$E^{D}_{tot} = E^{D}_{m1}E^{D}_{m2}E^{D}_{m3}E^{D}_{\alpha1}E^{D}_{\alpha2}[p_{\beta1}E^{D}_{\beta1} + p_{\beta2}E^{D}_{\beta2}]\prod_x E_x \quad (14)$$

where D represents ^{2}H occupancy of a hydrogen site. $E^{D}_{\alpha n}$ is the waveform from coupling to the nth α-^{2}H site on C2, E^{D}_{mn} is the ESEEM waveform from coupling to the nth C5′ methyl hydrogen site, and $E^{D}_{\beta n}$ is the waveform from coupling to the nth β-^{2}H site on C1. Previous multifrequency three-pulse ESEEM studies[28,29] have shown that there are two populations of active sites that are distinguished by having different β-^{2}H hyperfine couplings. There is one type of β-H hyperfine coupling in each active site. The coupling with the C5′ methyl group appears to be identical in each type of site. The terms $E^{D}_{\beta1}$ and $E^{D}_{\beta2}$ represent the modulation from the β-^{2}H coupling in the two types of active site, and $p_{\beta1}$ and $p_{\beta2}$ are the corresponding relative populations, where $p_{\beta1} + p_{\beta2} = 1$. The term ΠE_X represents modulation from hyperfine coupling to nuclei other than the hydrogen sites defined above. The overall ESEEM waveform from the sample prepared by using natural abundance $^1H_4$-aminoethanol is given by the following expression:

$$E^{H}_{tot} = E^{H}_{m1}E^{H}_{m2}E^{H}_{m3}E^{H}_{\alpha1}E^{H}_{\alpha2}[p_{\beta1}E^{H}_{\beta1} + p_{\beta2}E^{H}_{\beta2}]\prod_x E_x \quad (15)$$

where H represents ^{1}H occupancy of the hydrogen sites defined above. Envelope-dividing eq 14 by eq 15 gives the following total ESEEM quotient waveform:

$$E^{Q}_{tot} = \frac{E^{D}_{m1}E^{D}_{m2}E^{D}_{m3}E^{D}_{\alpha1}E^{D}_{\alpha2}[p_{\beta1}E^{D}_{\beta1} + p_{\beta2}E^{D}_{\beta2}]}{E^{H}_{m1}E^{H}_{m2}E^{H}_{m3}E^{H}_{\alpha1}E^{H}_{\alpha2}[p_{\beta1}E^{H}_{\beta1} + p_{\beta2}E^{H}_{\beta2}]} \quad (16)$$

Note that ΠE_X is eliminated in eq 16, so that the quotient modulation does not include interfering contributions from hyperfine couplings that are common to the ^{2}H- and ^{1}H-labeled product radical states.

ESEEM Fitting. For a particular pair of experimental and calculated waveforms at the same magnetic field, a set of A and k values could be determined that gave the minimum possible σ value for the waveform fit, denoted σ_τ. In the determination of σ_τ, a value of $B = 0$ was used. The 250 τ values from 192 to 1686 ns were used to calculate σ_τ, which included the dominant modulation amplitude and avoided the poor signal-to-noise ratio region at $\tau > 1686$ ns. The waveform was further processed by removing a best-fit first-order polynomial from the data, followed by reconstruction of the dead time.[46] ESEEM frequency spectra were obtained from the processed waveform by discrete Fourier transformation by using Matlab's fft algorithm, and taking the real part (cosine Fourier transform) of the result.[39,55] Processed experimental data for τ values from 0 to 2274 ns were used to calculate the frequency domain spectra. No rescaling or offsets of the Fourier transforms were performed. Therefore, in the calculation of the minimum σ for fitting the Fourier transforms, σ_f, values of $A = 1$ and $B = 0$ were used. The 117 frequencies from 0.49 to 9.9 MHz were used in calculating σ_f, because the Fourier transform was distorted by truncation artifacts near the origin and the range of frequencies <10 MHz included all ^{2}H features above the signal-to-noise.

The "goodness-of-fit" for the global (four magnetic field values) ESEEM simulations was assessed from the value of σ_{ESE}, which was a product of two factors: (1) the sum of four σ_τ values (one for each magnetic field used) and (2) the product of four σ_f values (one for each magnetic field used). Other combinations of sums and products of σ_τ and σ_f values were tried, but optimization of the $\sigma_{ESE} = (\Sigma\sigma_\tau)(\Pi\sigma_f)$ parameter led to the visually most appealing fits. The following parameters composed the adjustable parameter set that was varied to minimize the value of σ_{ESE}: (a) α and γ, the Euler angles used to orient the methyl group (β is determined by the values of θ_5 and ϕ_5), (b) θ_5, ϕ_5, the spherical coordinate position for C5′, with C2 at the origin, (c) θ_c, ϕ_c, the spherical coordinate position

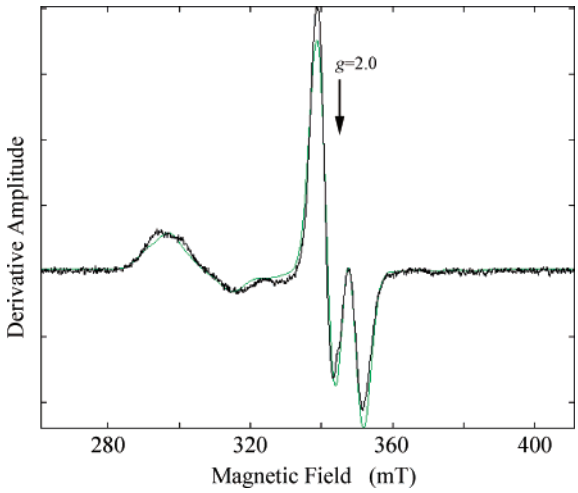

Figure 4. X-band continuous-wave EPR spectrum of the Co^{II}−product radical pair intermediate cryotrapped in ethanolamine deaminase (black line) and simulation (green line). The transitions associated with Co^{II} are prominent in the $g_\perp$ region around 300 mT. The product radical doublet line shape appears at 330−360 mT. The product radical was formed from $^2H_4$-aminoethanol. The free electron resonance position at $g = 2.0$ is shown by the arrow. *Experimental conditions:* microwave frequency, 9.6553 GHz; temperature, 6 K; microwave power, 2.0 mW; magnetic field modulation, 1.0 mT; modulation frequency, 100 kHz; scan rate, 0.75 mT/s; time constant, 0.2 s; average of 8 individual spectra minus the average of 4 baseline spectra. *Simulation parameters: J*, -67.2×10^{-4} cm^{-1}; *R*, 9.26 Å; line widths, 5.16 mT (radical), 6.08 mT (Co^{II}); *g* (radical), 2.000; $g_\perp$ (Co^{II}), 2.260; $g_{||}$ (Co^{II}), 2.010; $A_\perp$ (Co^{II}), 10×10^{-4} cm^{-1}; $A_{||}$ (Co^{II}), 103×10^{-4} cm^{-1}; Co^{II} scale factor, 1.

for Co^{II}, with C2 at the origin, (d) the C2−C5′ separation distance, (e) the C2−H_a separation distance, (f) $A_{iso,a}$, (g) $A_{iso,\beta 1}$, and (h) $r_{\beta 1}$. All other hyperfine coupling and atom position parameters reported in the text, Table 2, and Figure S1, with the exception of the fixed parameters, were derived from the model determined by these eight sets of adjustable parameters.

Results

EPR Spectroscopy. Figure 4 shows the experimental continuous-wave powder EPR spectrum of the Co^{II}−product radical pair state, obtained at 6 K. The state was generated by enzyme turnover on $^2H_4$-aminoethanol. The region of greatest Co^{II} intensity around 300 mT corresponds to the $g_\perp = 2.26$ position of the Co^{II} transitions in free cob(II)alamin.[60,61] The EPR transition intensity associated with the product radical appears at 330−360 mT, around $g = 2.0$. The doublet splitting of the radical line shape, which is only partially resolved, arises from the coupling of the unpaired electron spins localized on Co^{II} and C2.[8,26,51] An examination of the dependence of Co^{II}−radical pair line shapes on *J* has been reported.[62] The doublet splitting generally increases as $|J|$ rises. Simulations show that, for $J = 0$ and $R \geq 9$ Å, the doublet merges into a single peak.

Figure 4 also shows the simulated EPR line shape overlaid with the experimental spectrum. The agreement between the experimental and simulated line shapes is very good. The best-fit EPR parameters and their ranges are listed in Table 1. The fit shows a best-fit basin of attraction for *J* values from −212 to −191 MHz and *R* values from 8.49 to 10.50 Å. The overlap of the low- and high-field features of the radical doublet interferes with assessment of the *R*-dependent width of the individual features, and contributes to the relatively large range of *R*. An empirical expression was derived by Coffman and Buettner[63] to relate *J* and *R* for radical pairs, as follows

$$|J| \leq 4.05 \times 10^{11} e^{-1.8R} \quad (17)$$

where $|J|$ is in MHz and *R* is in Å. A value of $|J|$ in the range 191−212 MHz gives $R \leq 11.9$ Å, which is consistent with $8.49 \leq R \leq 10.50$ Å. The best-fit *J* and *R* values of −202 MHz and 9.26 Å are comparable to values obtained for simulation of the $g \approx 2$ region of the product radical pair line shape (antiferromagnetic, $J = -176$ to −164 MHz, $R = 9.4-10.0$ Å).[26] The *J* and *R* values for the Co^{II}−product radical pair are also comparable to the values determined for the Co^{II}−substrate radical pair state in ethanolamine deaminase from Clostridium ($|J| = 240$ MHz, antiferromagnetic; $R = 10-12$ Å)[27] and for the enzyme from *S. typhimurium* reported by two groups: $|J| = 196$ MHz, antiferromagnetic, $R = 11$ Å;[7] $|J| = 324$ MHz, antiferromagnetic, $R = 11$ Å.[23]

Magnetic Field Dependence of the Product Radical EPR Line Shape at Different Orientations. The calculated spectral contributions to the product radical EPR line shape from different single orientations, θ, of the electron−electron vector **R** relative to $\mathbf{B}_0$ are shown in Figure 5. In Figure 5, the upper left panel shows the calculated (eq 3) best-fit powder EPR absorption spectrum, $\langle f(\theta) \rangle$. Figure 5 also shows curves for the magnetic field dependence of the EPR transition probability, $f(\theta)$, calculated at selected individual θ values. The dark curves show the result of including the sin θ solid angle weighting factor, from the powder-average in eq 3. The dark curves correspond to the contributions of different orientations to the powder EPR spectrum. Figure 5 shows that contributions from orientations of **R** along $\mathbf{B}_0$ ($\theta \leq 30°$) are concentrated in the center of the product radical doublet line shape. In contrast, transitions from perpendicular orientations of **R** and $\mathbf{B}_0$ appear in the low- and high-field wings of the doublet.

Orientation Dependence of the Product Radical EPR Line Shape at Different Magnetic Fields. Figure 6 shows the contribution of different orientations, θ, to the EPR spectrum, at the four magnetic field values at which ESEEM was collected (discussed below). In Figure 6, the curve at each magnetic field value represents the normalized $P(\theta)$ values. The dark curves include the sin θ weighting factor, so that they reflect the overall contribution that each orientation makes to the powder average. The low-amplitude sharp features at $\theta = 17-18°$, 32−34°, and 42−43° in Figure 6 are caused by the reassignment of transitions between Co^{II} and radical in MENO and the different line widths used for Co^{II} and radical. A detailed description of these features for the substrate radical and a table of the transitions involved has been presented.[23]

The $P(\theta)$ sin θ curves in Figure 6 reflect the relative spin population at each orientation and can therefore be used as in eq 5 to weight the ESEEM powder averages. The EPR simulation results presented in Figures 5 and 6 show that the low-field edge of the radical EPR line shape is dominated by nearly perpendicular orientations of the Co^{II}−C2 vector, **R**, relative to $\mathbf{B}_0$. Therefore, the hyperfine line shapes in an ESEEM experiment performed at 306.0 mT on the low-field edge will be representative of these orientations. The same is true for the magnetic field of 319.0 mT at the high-field edge of the doublet. The central region of the radical EPR line shape around 313.3 mT corresponds to the overlap of the high-field edge of the larger amplitude low-field Pake doublet feature and the low-field edge of the high-field Pake doublet feature. Therefore, the intensity is dominated by orientations of **R** that are more nearly parallel to $\mathbf{B}_0$. At 310.5 mT, the full range of Co^{II}−C2 versus $\mathbf{B}_0$ orientations are sampled, and the ESEEM spectrum will correspond closely to a powder pattern.

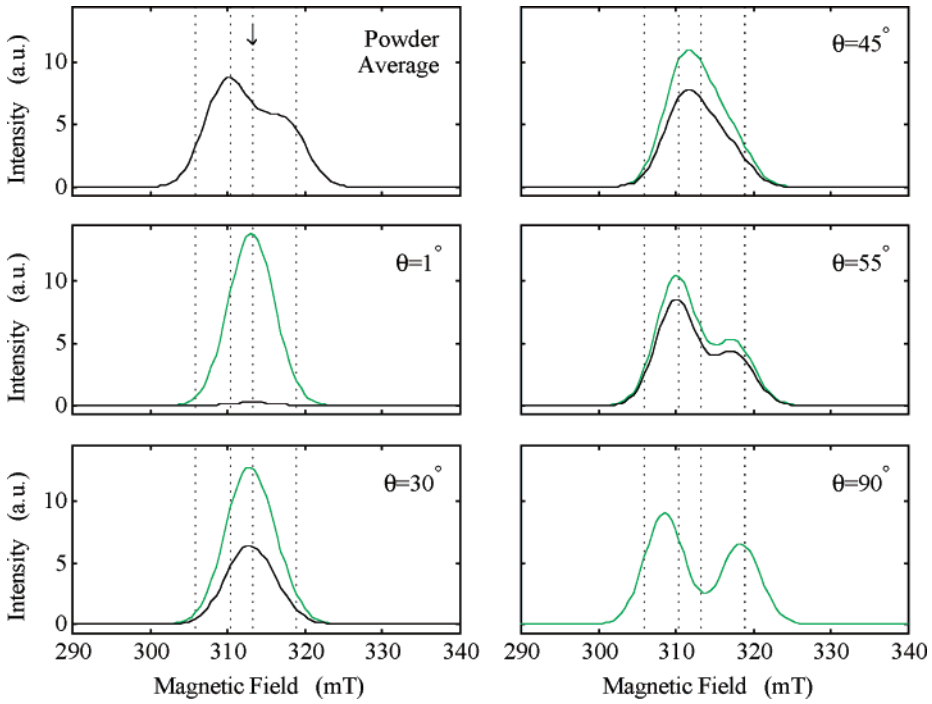

Figure 5. Powder average [$\langle f(\theta)\rangle$] and single orientation [$f(\theta)$] EPR absorption spectrum simulations for the product radical intermediate in ethanolamine deaminase. The four vertical dotted lines mark the magnetic field values at which ESEEM was collected. The light-line spectra represent $f(\theta)$ and the heavy lines correspond to $f(\theta)$ weighted by sin θ. The free electron resonance position at $g = 2.0$ is shown by the arrow in the top left panel. *Simulation parameters:* J, -67.2×10^{-4} cm^{-1}; R, 9.26 Å; line widths, 5.16 mT (radical), 6.08 mT (Co^{II}); g (radical), 2.000; $g_\perp$ (Co^{II}), 2.260; $g_\parallel$ (Co^{II}), 2.010; $A_\perp$ (Co^{II}), 10×10^{-4} cm^{-1}; $A_\parallel$ (Co^{II}), 103×10^{-4} cm^{-1}; Co^{II} scale factor, 0; frequency, 8.768 GHz.

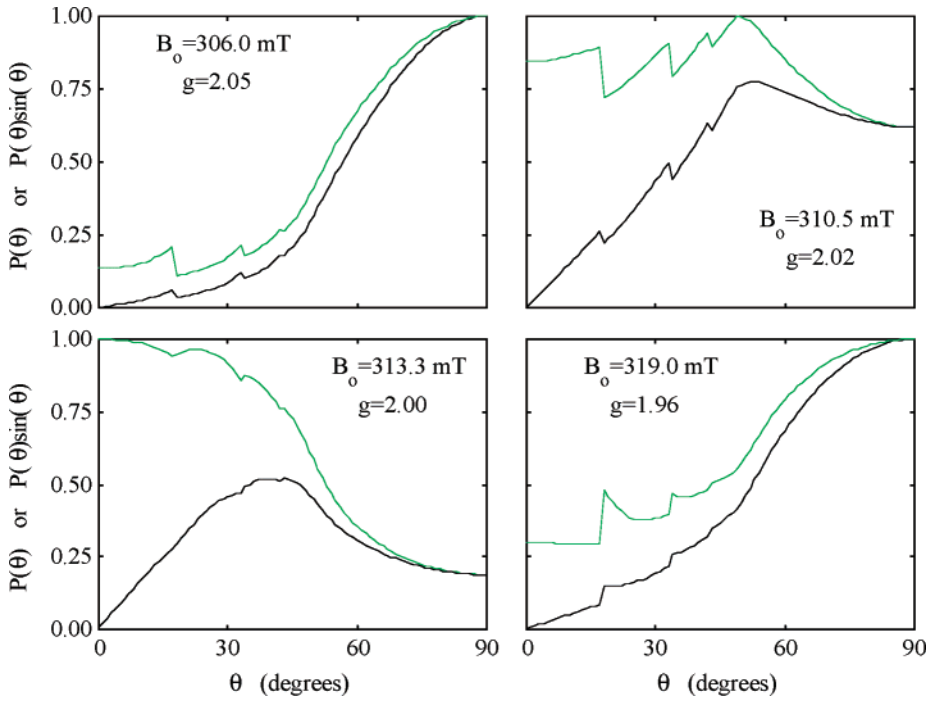

Figure 6. Relative contributions of orientations, θ, to the EPR transition intensity of the product radical intermediate in ethanolamine deaminase at the four values of fixed magnetic field used for ESEEM. The light-line spectra represent $P(\theta)$ and the heavy lines correspond to $P(\theta)$ weighted by sin θ. *Simulation parameters:* J, -67.2×10^{-4} cm^{-1}; R, 9.26 Å; line widths, 5.16 mT (radical), 6.08 mT (Co^{II}); g (radical), 2.000; $g_\perp$ (Co^{II}), 2.260; $g_\parallel$ (Co^{II}), 2.010; $A_\perp$ (Co^{II}), 10×10^{-4} cm^{-1}; $A_\parallel$ (Co^{II}), 103×10^{-4} cm^{-1}; Co^{II} scale factor, 0; frequency, 8.768 GHz.

Magnetic Field Dependence of the Experimental ESEEM. Figure 7 shows two-pulse ESEEM collected at the four magnetic field values of 306.0, 310.5, 313.3, and 319.0 mT. The waveforms are the quotients of the waveforms from a ^{2}H-labeled sample (dividend) and natural isotope abundance, essentially ^{1}H-labeled, sample (divisor). The quotient ESEEM contains contributions from ^{2}H nuclei exchanged onto C5′, and the ^{1}H nuclei that were replaced. Modulation from the weakly-coupled matrix ^{1}H nuclei[64] is eliminated by the envelope division. For the $\mathbf{B}_0$ range from 306.0 to 319.0 mT, the free ^{2}H resonant frequency, ν_{2H}, varies from 2.00 to 2.08 MHz. The dominant oscillations with period 250−500 ns, arise from ^{2}H coupling.

The amplitude of the individual envelopes from the ^{2}H and ^{1}H samples decays quasi-exponentially as a function of τ with

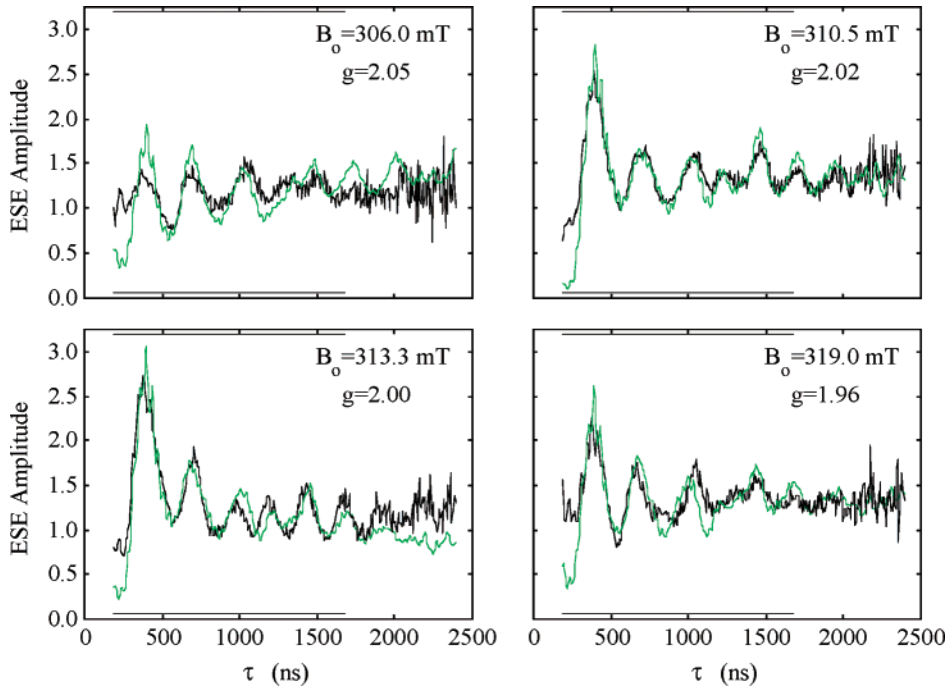

Figure 7. Experimental two-pulse ^{2}H/^{1}H quotient ESEEM collected for the product radical in ethanolamine deaminase at four different magnetic field values (black lines), and corresponding overlaid simulations (green lines). The dark horizontal bars mark the data range of τ (192 to 1686 ns) used in the fitting procedure. (A) $B_0 = 306.0$ mT. (B) $B_0 = 310.5$ mT. (C) $B_0 = 313.3$ mT. (D) $B_0 = 319.0$ mT. *Experimental conditions:* temperature, 6 K; microwave frequency, 8.768 GHz; microwave pulse power, 63 W; initial τ value, 192 ns; τ increment, 6 ns; $\pi/2$ pulse width, 20 ns; pulse repetition rate, 80 Hz; 100 repetitions averaged per point; average of at least seven envelopes for $^2H_4$ and at least sixteen envelopes for $^1H_4$ samples. *Simulation parameters: J*, -67.2×10^{-4} cm^{-1}; *R*, 9.26 Å; line widths, 5.16 mT (radical), 6.08 mT (Co^{II}); g (radical), 2.000; $g_\perp$ (Co^{II}), 2.260; $g_{||}$ (Co^{II}), 2.010; $A_\perp$ (Co^{II}), 10×10^{-4} cm^{-1}; $A_{||}$ (Co^{II}), 103×10^{-4} cm^{-1}; Co^{II} scale factor, 0. *Simulation fitting parameters:* All as defined in eqs 6, 7, and 9 (with $B = 0$) and (A) $\sigma_t = 14.0$, $k = 1.41 \times 10^{-4}$ ns^{-1}, $A = 1.88$, (B) $\sigma_t = 11.2$, $k = -6.25 \times 10^{-6}$ ns^{-1}, $A = 2.58$, (C) $\sigma_t = 10.3$, $k = -3.06 \times 10^{-4}$ ns^{-1}, $A = 3.23$, and (D) $\sigma_t = 16.7$, $k = -1.88 \times 10^{-5}$ ns^{-1}, $A = 2.61$.

a characteristic phase memory time given by $T_m \approx 1$ μs. Therefore, the signal amplitude and signal-to-noise ratio is lowest for large $\tau > 1.6$ μs, and this large relative noise at large τ is enhanced by the envelope division. The differences among the ESEEM collected at different magnetic field values show that orientation selection is present.

The cosine Fourier transforms of the ESEEM shown in Figure 7 are presented in Figure 8. The intensity in the spectral region $\leq$10 MHz is dominated by features arising from ^{2}H hyperfine coupling. Significant intensity from the ^{1}H coupling appears at ν_{1H} (13−14 MHz) and $2\nu_{1H}$ (26−27 MHz) and is therefore not shown in the spectral range of Figure 8. The amplitudes of features in the ESEEM spectra vary significantly with magnetic field, but the frequency ranges of the transitions are comparable, and in common with the frequency positions of features observed in the powder three-pulse ESEEM spectra collected at $g = 2.02$.[29] Thus, as assigned previously,[29] the single narrow feature at ν_{2H} arises from two weakly coupled ^{2}H nuclei. The pair of features that are split symmetrically about ν_{2H} by approximately 1.4 MHz arise from a single strongly coupled ^{2}H nucleus. The intensity in the spectral region 3.5−6.0 MHz arises from two contributions. The positive intensity in the region 3.5−6.0 MHz is the $m_s = +^1/_2$ feature from coupling between the electron spin at C2 and one β-^{2}H nucleus bonded to C1 ($^2H_{\beta 1}$). Intensity from the $m_s = -^1/_2$ conjugate feature is partially obscured by the baseline disturbance at the beginning of the Fourier transform. The depression at frequencies 0.2−0.3 MHz above $2\nu_{2H} = 4.0$−4.2 MHz (for $B_0 = 306.0$−319.0 mT) is the negative phase sum-combination feature of the strongly coupled C5′-methyl ^{2}H nucleus. The shift of the sum combination line from $2\nu_{2H}$ is consistent with the large dipolar contribution to this hyperfine coupling.[65] As expected from previous three-pulse ESEEM studies,[29] features from the $H_{\beta 2}$ coupling are too weak to observe above the experimental noise level under the microwave field and magnetic field conditions of 8.8 GHz and 306.0−319.0 mT used in the present experiments.

Simulation of the ESEEM. Figure 7 shows simulated quotient two-pulse ESEEM overlaid with the corresponding experimental waveforms. The best-fit parameter set used for the calculated ESEEM was obtained from the global simulation of the ESEEM collected at the four magnetic field values. The best fit parameters and the parameter ranges are listed in Table 2. Simulation fitting parameters (A, k, and associated σ_t values) are presented in the legend to Figure 7. The ranges in Table 2 were obtained by pooling a list of parameter values and fit numbers for 71 370 fitting attempts (simulation runs), choosing a cutoff fit number, and then listing the range of each parameter that gave a fit number below the cutoff. Plots of fit numbers versus parameter value for the different parameters are included in Supporting Information, Figure S1. Table 2 shows that there are two possible values for the Co^{II}−C5′ distance, 6.3 and 12.5 Å, because, owing to the symmetry of the atom arrangement shown in Figure 3, the Co^{II}−C2 vector can be reversed without altering the ESEEM. The two distances are distinguished by additional considerations, as described below.

The $A_{iso,n}$ and atom−atom distance parameters from the orientation-selection two-pulse ESEEM are comparable with the corresponding values obtained from simulations of the powder three-pulse ESEEM.[29] As given in Table 2, the values of $A_{iso,a} = -0.75$ MHz and $r_a = 2.42$, $r_b = 4.07$, and $r_c = 4.09$ Å are the same within error as the values of $A_{iso,1} = -0.9$ MHz and $r_a = 2.3$, $r_b = r_c = 4.2$ Å obtained in the powder three-pulse ESEEM study.[29] The $A_{iso,\beta 1}$ and $r_{\beta 1}$ values in Table 2 are also the same within error as the corresponding values of 4.7 MHz

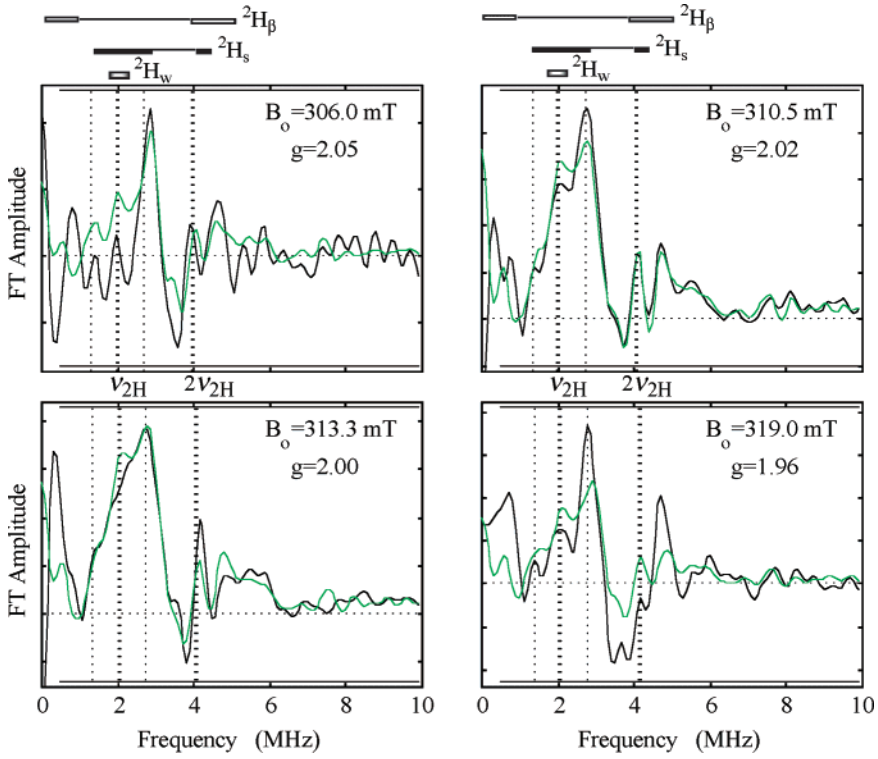

Figure 8. Fourier transforms of the two-pulse $^2H/^1H$ quotient ESEEM collected from the product radical in ethanolamine deaminase at four different magnetic field values (black lines), and corresponding overlaid simulations (green lines). Features arising from the strongly coupled ^2H (^2H_s), the two weakly coupled ^2H (^2H_w), and the observed β-^2H ($^2H\beta_1$) are noted. The dark horizontal bars mark the range of frequencies (0.49−9.9 MHz) used in the fitting procedure. The four vertical lines are at the frequencies $\nu_{2H} = B_0 \times 6.53566$ MHz/T, $\nu_{2H} \pm 0.7$ MHz, and $2\nu_{2H}$. *Experimental conditions:* Same as described in the legend of Figure 7. *Simulation fitting parameters:* All as defined in eq 7 (with $A = 1$ and $B = 0$) and (A) $\sigma_f = 8.95 \times 10^3$, (B) $\sigma_f = 244$, (C) $\sigma_f = 304$, and (D) $\sigma_f = 5.36 \times 10^3$.

and 2.5 Å for $^2H_{\beta 1}$ obtained in the powder three-pulse ESEEM study.[29] In addition, the sum of the $\theta_{\beta 1}$ and $\theta_{\beta 2}$ values corresponding to the adjustable $A_{iso,\beta 1}$ parameter and fixed $A_{iso,\beta 2}$ value is 121°, which is consistent with the value of 120° expected for the angular displacement of $H_{\beta 1}$ and $H_{\beta 2}$ about the C1−C2 axis, because C1 is sp^3-hybridized.[28] A value of 120° was previously obtained in the powder three-pulse ESEEM study.[28,29]

Figure 8 shows the simulated frequency spectra, obtained by Fourier transforming the ESEEM in Figure 7, overlaid with the corresponding experimental Fourier transforms. For the C5′ ^2H couplings, the simulations reproduce the growth and broadening of the feature from the weakly coupled ^2H (H_b, H_c, or H_w) centered at ν_{2H}, and the dramatic changes in the asymmetric line shape of the strongly coupled ^2H (H_a or H_s), that are associated with the increase in magnetic field from 306.0 to 313.3 mT. The interplay between the magnetic field-dependent β-^2H intensity and the overlapping negative phase of the ^2H_s sum combination line is also reproduced.

Discussion

Model for the Geometry of Reactant Centers in the Active Site. Figure 9 shows the model for the geometry of the reactant centers in the active site in the Co^{II}−product radical pair state of ethanolamine deaminase, which is based on the best-fit parameter values presented in Tables 1 and 2. The value of $R = 9.3$ Å for the Co^{II}−C2 distance is obtained from the EPR simulations. The global best-fit ESEEM simulation parameters establish the relative positions of Co^{II}, C2, C1, and the C5′-methyl group. In the model, C5′ is placed between Co^{II} and C2, which corresponds to selection of the Co^{II}−C5′ distance of 6.3 Å given in Table 2. This is consistent with the shortest-distance path for the migrating C5′ radical center between Co^{II} and the substrate/product binding site. A position of C5′ between Co^{II} and C2 is also consistent with X-ray crystallographic structures of coenzyme B_{12}-dependent enzymes,[10−19] which indicate that the space above the β-face of the cobalamin between cobalt and the substrate is relatively free, whereas displacement of C5′ beyond the bound substrate (or inhibitors or products) is restricted by the protein that forms the side of the substrate binding site distal to Co^{II}. The C5′-methyl and C2-methylene groups are at closest van der Waals contact. C5′ lies slightly off of the Co^{II}−C2 axis, corresponding to a perpendicular distance, $r_\perp$, of 1.6 Å (range 0.1−2.1 Å) and an angle between the Co^{II}−C2 and C5′−C2 axes of 27°. Other notable orientations in the model include the C5′−H_a−C2 angle of 161° (angular range of 143−180°), which indicates that this group of centers is nearly linear. The C1−C2 axis of the product radical makes an angle of 50° (angular range of 46−85°) with the Co^{II}−C2 axis.

Implications for the Mechanism of Catalysis. The process of radical pair recombination from the Co^{II}−product radical pair state to the diamagnetic adenosylcob(III)alamin−product state is mediated by migration of the C5′ radical center of the deoxyadenosyl group,[29] as inferred earlier from the studies of the substrate radical state.[21−23] The model in Figure 9 indicates that C5′ undergoes a displacement during radical pair recombination of at least 4.3 Å, from the position near the product radical to the bonded position 2.0 Å from the cobalt atom[66] in adenosylcob(III)alamin. This distance is shorter than the radical pair separation distance of 6.0 Å that was concluded from the orientation-selection ESEEM study of the Co^{II}−substrate radical intermediate.[23] The shorter distance for radical migration determined from the Co^{II}−product radical pair state arises from

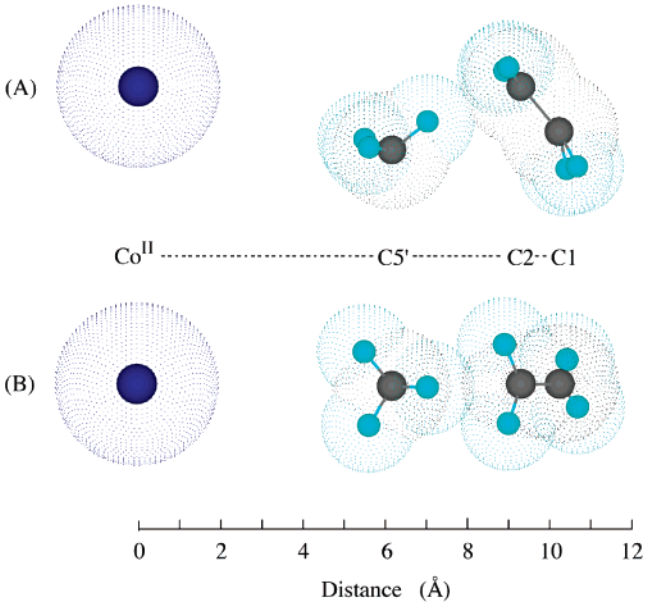

Figure 9. Model for the structure of the reactant centers in the active site of the Co^{II}−product radical pair state in ethanolamine deaminase. (A) View along the line perpendicular to the Co^{II}−C2−C1 plane. (B) View after 90° rotation about the Co^{II}−C2 axis, relative to view in (A). The positions of Co^{II} (dark blue), C1, C2, C5′ (charcoal), and the C5′-methyl hydrogen atoms (light blue) are marked by small spheres. The dotted surfaces represent the extent of the van der Waals radii of the atoms. The positions and orientations of the atom centers are to scale, relative to the plane of the Co^{II}−C2 axis, which lies in the plane of the page. The distance scale corresponds to the Co^{II}−C2 axis on the plane of the page. In (A), H_c, $H_{\alpha 1}$, and $H_{\beta 1}$ are in the foreground, and H_b, $H_{\alpha 2}$ and $H_{\beta 2}$ are in the background. In (B), H_c, $H_{\alpha 1}$, and $H_{\beta 1}$ are near the bottom, and H_b, $H_{\alpha 2}$, and $H_{\beta 2}$ are near the top.

the shorter Co^{II}−C2 distance of 9.3 Å (range of 8.5−10.5 Å), relative to the Co^{II}−C1 distance of 11.1 Å (range of 10.9−11.5 Å)[23] obtained for the Co^{II}−substrate radical pair state. The orientation of the C2−C1 axis relative to the Co^{II}−C2 axis in Figure 9 supports the EPR simulation result that C1 is more distant from Co^{II} than C2. The model presented in Figure 9, along with the assumption that the positions of the C1 and C2 atoms in the substrate and product radical states are comparable, suggests that radical pair separation may occur over a distance that is 1−2 Å farther than radical pair recombination. The small shift of the C5′-methyl group from the position determined in the substrate radical state to the position in the product radical state must occur during or after migration of the amine from C2 to C1.

The best-fit [C5′−H_a···C2•] angle of 161°, as given in Table 2 and shown in Figure 9, suggests that the second hydrogen atom transfer from the C5′-methyl group to C2 (HT2 in Figure 2) proceeds with a nearly in-line arrangement, and therefore a transition state with predominantly linear character. The approximately perpendicular orientation of the C2−C1 and C5′−C2 axes is also consistent with a nearly linear transition state. In this orientation, the p-orbital on C2 that accepts the hydrogen atom is pointing along the C5′−H_a axis.

Figure 9 shows that the plane defined by the $H_{\alpha 1}$, $H_{\alpha 2}$, C2, and C1 atoms defines sides of the product radical that face toward or away from Co^{II}. The radical migration and hydrogen atom transfer reactions occur on the side of the plane facing Co^{II}. Amine migration occurs on the side of the plane facing away from Co^{II}. The partitioning of the subreactions into separate spatial regions of the active site would allow specialization of the protein structures that guide these distinctive processes and also eliminate interference between the reactions.

Acknowledgment. Supported by grant R01 DK54514 from the National Institutes of Health. We thank Ms. Lori Anderson for technical assistance, and Professor Dale E. Edmondson (Emory University) for use of fermentation facilities. Calculations were performed, in part, using computer resources at the Emerson Center for Scientific Computation at Emory University, which is funded by National Science Foundation grant CHE-0079627 and an IBM Shared University Research Award.

Supporting Information Available: Plots of fitting function values for individual parameters. This material is available free of charge via the Internet at http://pubs.acs.org.

References and Notes

(1) Bandarian, V.; Reed, G. H. Ethanolamine Ammonia-Lyase. In *Chemistry and Biochemistry of B12*; Banerjee, R., Ed.; John Wiley and Sons: New York, 1999; p 811.
(2) Bradbeer, C. *J. Biol. Chem.* **1965**, *240*, 4669.
(3) *B12*; Dolphin, D., Ed.; Wiley: New York, 1982; Vol. 2.
(4) Buckel, W.; Golding, B. T. *Chem. Soc. Rev.* **1996**, *25*, 329.
(5) Banerjee, R. *Chemistry and Biochemistry of B12*; John Wiley and Sons: New York, 1999.
(6) Babior, B. M.; Moss, T. H.; Orme-Johnson, W. H.; Beinert, H. *J. Biol. Chem.* **1974**, *249*, 4537.
(7) Bandarian, V.; Reed, G. H. *Biochemistry* **2002**, *41*, 8580.
(8) Warncke, K.; Schmidt, J. C.; Ke, S.-C. *J. Am. Chem. Soc.* **1999**, *121*, 10522.
(9) Licht, S. S.; Lawrence, C. C.; Stubbe, J. *J. Am. Chem. Soc.* **1999**, *121*, 7463.
(10) Mancia, F.; Keep, N. H.; Nakagawa, A.; Leadlay, P. F.; McSweeney, S.; Rasmussen, B.; Bösecke, P.; Diat, O.; Evans, P. R. *Structure* **1996**, *4*, 339.
(11) Mancia, F.; Evans, P. R. *Structure* **1998**, *6*, 711.
(12) Mancia, F.; Smith, G. A.; Evans, P. R. *Biochemistry* **1999**, *38*, 7999.
(13) Reitzer, R.; Gruber, K.; Jogl, G.; Wagner, U. G.; Bothe, H.; Buckel, W.; Kratky, C. *Structure* **1999**, *7*, 891.
(14) Gruber, K.; Reitzer, R.; Kratky, C. *Angew. Chem., Int. Ed. Engl.* **2001**, *40*, 3377.
(15) Shibata, N.; Masuda, J.; Tobimatsu, T.; Toraya, T.; Suto, K.; Morimoto, Y.; Yasuoka, N. *Structure* **1999**, *7*, 997.
(16) Masuda, J.; Shibata, N.; Morimoto, Y.; Toraya, T.; Yasuoka, N. *Structure* **2000**, *8*, 775.
(17) Yaminishi, M.; Yunoki, M.; Tobimatsu, T.; Sato, H.; Matsui, J.; Dokiya, A.; Iuchi, Y.; Oe, K.; Suto, K.; Shibata, N.; Morimoto, Y.; Yasuoka, N.; Toraya, T. *Eur. J. Biochem.* **2002**, *269*, 4484.
(18) Liao, D.-I.; Dotson, G.; Turner, I.; Reiss, L.; Emptage, M. *J. Inorg. Biochem.* **2003**, *93*, 84.
(19) Sintchak, M. D.; Arjara, G.; Kellogg, B. A.; Stubbe, J.; Drennan, C. L. *Nature Struct. Biol.* **2002**, *9*, 293.
(20) Champloy, F.; Jogl, G.; Reitzer, R.; Buckel, W.; Bothe, H.; Beatrix, B.; Broeker, G.; Michalowicz, A.; Meyer-Klaucke, W.; Kratky, C. *J. Am. Chem. Soc.* **1999**, *121*, 11780.
(21) Lobrutto, R.; Bandarian, V.; Magnusson, O. T.; Chen, X.; Schramm, V. L.; Reed, G. H. *Biochemistry* **2001**, *40*, 9.
(22) Warncke, K.; Utada, A. S. *J. Am. Chem. Soc.* **2001**, *123*, 8564.
(23) Canfield, J. M.; Warncke, K. *J. Phys. Chem. B* **2002**, *106*, 8831.
(24) Faust, L. P.; Connor, J. A.; Roof, D. M.; Hoch, J. A.; Babior, B. M. *J. Biol. Chem.* **1990**, *265*, 12462.
(25) Faust, L. P.; Babior, B. M. *Arch. Biochem. Biophys.* **1992**, *294*, 50.
(26) Ke, S.-C. *Biochim. Biophys. Acta* **2003**, *1620*, 267.
(27) Boas, J. F.; Hicks, P. R.; Pilbrow, J. R.; Smith, T. D. *J. Chem. Soc., Faraday II* **1978**, *74*, 417.
(28) Warncke, K.; Canfield, J. M. *J. Am. Chem. Soc.* **2004**, *126*, 5930.
(29) Warncke, K. *Biochemistry*, in press.
(30) Press, W. H.; Teukolsky, S. A.; Vetterling, W. T.; Flannery, B. P. *Numerical Recipes in C: The Art of Scientific Computing*, 2nd ed.; Cambridge University Press: New York, 1992.
(31) Lagarias, J. C.; Reeds, J. A.; Wright, M. H.; Wright, P. E. *SIAM J. Optimization* **1998**, *9*, 112.
(32) Rist, G. H.; Hyde, J. S. *J. Chem. Phys.* **1970**, *52*, 4633.
(33) Hoffman, B. M.; Martinsen, J.; Venters, R. A. *J. Magn. Reson.* **1984**, *59*, 110.
(34) Hoffman, B. M.; Venters, R. A.; Martinsen, J. *J. Magn. Reson.* **1985**, *62*, 537.
(35) Hoffman, B. M.; DeRose, V. J.; Doan, P. E.; Gurbiel, R. J.; Houseman, A. L. P.; Telser, J. I., Volume., Eds., pp. Metalloenzyme active-site structure and function through multifrequency cw and pulsed ENDOR.

In *Biological Magnetic Resonance*; Berliner, L. J., Reuben, J., Eds.; Plenum Press: New York, 1993; Vol. 13, p 151.

(36) Lee, H.-I.; Doan, P. E.; Hoffman, B. M. *J. Magn. Reson.* **1999**, *140*, 91.

(37) Bandarian, V.; Poyner, R. R.; Reed, G. H. *Biochemistry* **1999**, *38*, 12403.

(38) Wertz, J. E.; Bolton, J. R. *Electron Spin Resonance*; Chapman and Hall: New York, 1986.

(39) Dikanov, S. A.; Tsvetkov, Y. D. *Electron Spin−Echo Envelope Modulation (ESEEM) Spectroscopy*; CRC Press: Boca Raton, FL, 1992.

(40) Deligiannakis, Y.; Louloudi, M.; Hadjiliadis, N. *Coord. Chem. Rev.* **2000**, *204*, 1.

(41) Schweiger, A.; Jeschke, G. *Principles of pulse electron paramagnetic resonance*; Oxford University Press: New York, 2001.

(42) Harkins, T.; Grissom, C. B. *J. Am. Chem. Soc.* **1995**, *117*, 566.

(43) Kaplan, B. H.; Stadtman, E. R. *J. Biol. Chem.* **1968**, *243*, 1787.

(44) Hollaway, M. R.; Johnson, A. W.; Lappert, M. F.; Wallis, O. C. *Eur. J. Biochem.* **1980**, *111*, 177.

(45) Bandarian, V.; Reed, G. H. *Biochemistry* **1999**, *38*, 12394.

(46) Mims, W. B. *J. Magn. Reson.* **1984**, *59*, 291.

(47) Eaton, S. S.; More, K. M.; Sawant, B. M.; Boymel, P. M.; Eaton, G. R. *J. Magn. Reson.* **1983**, *52*, 435.

(48) Canfield, J. M. Approaching magnetic field effects in biology using the radical pair mechanism, University of Illinois, Urbana-Champaign, 1997.

(49) Mims, W. B. *Phys. Rev. B* **1972**, *5*, 2409.

(50) Mims, W. B. *Phys. Rev. B* **1972**, *6*, 3543.

(51) Ke, S.-C.; Warncke, K. *J. Am. Chem. Soc.* **1999**, *121*, 9922.

(52) Gordy, W. *Theory and Applications of Electron Spin Resonance*; John Wiley & Sons: New York, 1980; Vol. XV.

(53) Heller, C.; McConnell, H. M. *J. Chem. Phys.* **1960**, *32*, 1535.

(54) Fessenden, R. W.; Schuler, R. H. *J. Chem. Phys.* **1963**, *39*, 2147.

(55) Kevan, L.; Bowman, M. K. *Modern Pulsed and Continuous Wave Electron Spin Resonance*; Wiley: New York, 1990.

(56) Stoll, S.; Schweiger, A. *J. Magn. Reson.* **2003**, *163*, 248.

(57) Rowan, L. G.; Hahn, E. L.; Mims, W. B. *Phys. Rev.* **1965**, *137*, A61.

(58) Kevan, L.; Schwartz, R. N. *Time Domain Electron Spin Resonance*; John Wiley and Sons: New York, 1979.

(59) Mims, W. B.; Davis, J. L.; Peisach, J. *J. Magn. Reson.* **1990**, *86*, 273.

(60) Pilbrow, J. R. EPR of B12-dependent enzyme reactions and related systems. In *B12*; Dolphin, D., Ed.; Wiley: New York, 1982; Vol. 1, p 431.

(61) Gerfen, G. J. EPR spectroscopy of B12-dependent enzymes". In: Chemistry and Biochemistry of B12. In *Chemistry and Biochemistry of B12*; Banerjee, R., Ed.; John Wiley and Sons: New York, 1999; p 165.

(62) Gerfen, G. J.; Licht, S.; Willems, J.-P.; Hoffman, B. M.; Stubbe, J. *J. Am. Chem. Soc.* **1996**, *118*, 8192.

(63) Coffman, R. E.; Buettner, G. R. *J. Phys. Chem.* **1979**, *83*, 2387.

(64) Hyde, J. S.; Rist, G. H.; Eriksson, L. E. G. *J. Phys. Chem.* **1968**, *72*, 4269.

(65) Astashkin, A. V.; Dikanov, S. A. In *Advanced EPR: Applications in Biology and Chemistry*; Hoff, A. J., Ed.; Elsevier: New York, 1989; p 59.

(66) Kratky, K.; Krautler, B. X-ray crystallography of B12. In *Chemistry and Biochemistry of B12*; Banerjee, R., Ed.; John Wiley and Sons: New York, 1999; p 9.

(67) Glusker, J. P. X-ray crystallography of B12 and cobaloximes. In *B12*; Dolphin, D., Ed.; Wiley: New York, 1982; Vol. 1, p 23.

(68) Ke, S.-C.; Torrent, M.; Museav, D. G.; Morokuma, K.; Warncke, K. *Biochemistry* **1999**, *38*, 12681.

(69) Abend, A.; Bandarian, V.; Nitsche, R.; Stupperich, E.; Retey, J.; Reed, G. H. *Arch. Biochem. Biophys.* **1999**, *370*, 138.

(70) Babior, B. M. Ethanolamine ammonia-lyase. In *B12*; Dolphin, D., Ed.; Wiley: New York, 1982; Vol. 2, p 263.